Delft University of Technology

Wavenumber-dependent dynamic light scattering optical coherence tomography measurements of collective and self-diffusion

Cheishvili, Konstantine; Besseling, Rut; Hermes, Michiel; Kalkman, Jeroen

Important note
To cite this publication, please use the final published version (if applicable).
Please check the document version above.

Wavenumber-dependent dynamic light scattering optical coherence tomography measurements of collective and self-diffusion

KONSTANTINE CHEISHVILI,[1] [ID] **RUT BESSELING,[2] MICHIEL HERMES,[2] AND JEROEN KALKMAN[1]**

[1]*Department of Imaging Physics, Delft University of Technology , Lorentzweg 1, 2628 CJ, Delft, The Netherlands*
[2]*InProcess-LSP, Kloosterstraat 9, 5349 AB, Oss, The Netherlands*

Abstract: We demonstrate wavenumber-dependent DLS-OCT measurements of collective and self-diffusion coefficients in concentrated silica suspensions across a broad q-range, utilizing a custom home-built OCT system. Depending on the sample polydispersity, either the collective or self-diffusion is measured. The measured collective-diffusion coefficient shows excellent agreement with hard-sphere theory and serves as an effective tool for accurately determining particle sizes. We employ the decoupling approximation for simultaneously measuring collective and self-diffusion coefficients, even in sufficiently monodisperse suspensions, using a high-speed Thorlabs OCT system. This enables particle size and volume fraction determination without the necessity of wavenumber-dependent measurements. We derive a relationship between the particle number-based polydispersity index and the ratio of self and collective mode amplitudes in the autocorrelation function and utilize it to measure the particle number-based polydispersity index. Notably, the polydispersity determined in this manner demonstrates improved sensitivity to smaller particle sizes compared to the standard intensity-based DLS cumulant analysis performed on dilute samples.

1. Introduction

Colloidal dispersions are widely used in chemical, pharmaceutical, and food industries, as well as in the domains of biology and medicine. Dynamic light scattering (DLS) is one of the most popular experimental techniques for studying colloidal systems [1–3]. It is a relatively simple and versatile technique that relies on the measurement of fluctuations in scattered light to obtain information about the diffusive motion of colloidal particles, predominantly used to obtain colloidal size characteristics. However, conventional DLS is limited to samples that are not in flow and have a low concentration of scatterers that have little multiple scattering. Dynamic light scattering optical coherence tomography (DLS-OCT) incorporates coherence gating to obtain a depth-resolved particle diffusion coefficient [4]. In DLS-OCT coherence gating suppresses multiple scattering and allows to study diffusive dynamics in more concentrated samples [5–7] and under flow [8–10].

In low-concentration particle suspensions, particle interactions are negligible, and the diffusion coefficient is inversely proportional to the particle hydrodynamic radius via the Stokes-Einstein relation. However, there is generally no such simple relation for concentrated samples. Concentrated particle suspension dynamics has been an active area of research for many years [11] and rheological models have been developed for highly concentrated charge-stabilized hard-sphere particle suspensions. These models describe particle diffusion through collective and self-diffusion mechanisms over short and long time scales [12–15]. Collective diffusion

describes the relaxation of concentration gradients over specific length scales and thus depends on the scattering wavenumber q, while self-diffusion describes the mean squared displacement (MSD) of individual colloid particles. Conventional DLS has been utilized to measure the collective and/or self-diffusion coefficient of concentrated hard-sphere particle suspensions using an index-matching procedure [16–18]. This is a non-trivial process that requires extensive sample preparation to minimize multiple scattering and make self-diffusion measurable. Two-color [11,14] or cross correlation [19] DLS has been employed to measure the collective diffusion coefficient over a large q-range in concentrated samples. While these methods effectively suppress multiple scattering, they require a more complex setup with at least two different scattering arms or wavelengths and involves laborious subsequent measurement of different incident and/or scattering vectors to obtain wavenumber-dependent dynamics.

In this work, we employ DLS-OCT to measure the q-dependent particle diffusion in dense suspensions in the spectral domain. DLS-OCT is generally used for conducting spatially resolved coherence-gated measurements of diffusion and flow by Fourier transformation over all wavenumbers. Nonetheless, when operated in the spectral domain, it can provide heterodyne correlation measurements at the different wavelengths of the OCT bandwidth and thus can be employed to simultaneously measure wavenumber-dependent diffusion over the entire bandwidth. This is akin to conducting parallel DLS measurements at different wavelengths or scattering angles. However, the limited spectral width of typical OCT systems makes the q-range relatively small. In this study, we employ a custom-built broad bandwidth DLS-OCT system to measure wavenumber-dependent dynamics in a single measurement over a large q-range. From the scattering wavenumber dependency of the decorrelation, we measured the long- and short-time collective and self-diffusion coefficients in concentrated silica suspensions in a straightforward manner and correlated them with particle size and polydispersity.

2. Theory

2.1. Particle diffusion

In dilute particle suspensions with a particle volume fraction $f_v \rightarrow 0$, direct and hydrodynamic interactions between the particles are negligible [20]. The diffusion coefficient for non-interacting particles undergoing Brownian motion is given by the Stokes-Einstein equation

$$D_0 = \frac{k_B T}{6\pi \eta_0 a},\tag{1}$$

where k_B is the Boltzmann constant, T is the absolute temperature, η_0 is the suspension dynamic viscosity, and a is the particle hydrodynamic radius. For charge-stabilized particle suspensions with a sufficient salt concentration, the hydrodynamic radius is the particle radius [16].

In concentrated suspensions, particle motion is affected by the presence of surrounding particles. For these suspensions we differentiate between short-time ($t \ll \tau_0$) and long-time ($t \gg \tau_0$) diffusive regimes, as well as between collective and self-diffusion. Here, t is the time over which the motion is probed (lag time in DLS-OCT correlation functions), while τ_0 is the interaction time defined as $\tau_0 = a^2/D_0$ [20,21]. In the short-time regime, particle motion is primarily influenced by solvent-mediated hydrodynamic interactions between the particles. In the long-time regime, excluded volume interactions and direct electrostatic interactions additionally affect the diffusion (in different ways for collective and self-diffusion and at different time scales). Self-diffusion pertains to the mean squared displacement of individual colloid particles, while collective diffusion involves the relaxation of concentration gradients across specific length scales. Dynamic light scattering (DLS) on a monodisperse particle suspension measures the collective diffusion coefficient for a particular length scale related to the wavelength and angle of the experiment [20].

In the dilute limit, there is no difference between the two different time scales or collective and self-diffusion. However, due to the interactions described above in concentrated systems, both collective and self-diffusion coefficients become functions of the particle volume fraction due to both hydrodynamic and direct interactions, and a function of time, represented by the transition from short to long-time dynamics [21–24]. Furthermore, the collective diffusion coefficient becomes a function of the scattering wavenumber, $q = 4\pi n \sin(\theta/2)/\lambda_0$, where λ_0 is the illuminating light wavelength, n is the suspension refractive index, and θ is the angle between the illumination and scattering directions. The wavenumber dependence of collective diffusion reflects the fact that, due to particle interactions, the diffusion of a density fluctuation in the suspension can strongly depend on the length scale of that fluctuation.

2.1.1. Self-diffusion

Self-diffusion describes how an individual particle diffuses in the presence of other Brownian particles. Therefore, it can only be detected when individual particles are optically distinguishable, either due to the polydispersity of particle scattering properties in the suspension, or by index-matching the majority of particles within the solvent, leaving only a small fraction of optically contrasting particles of interest that determine the scattered light fluctuations. Index matching ensures that the light-scattering particles do not interact with each other but do interact with other non light-scattering particles. Since self-diffusion depends solely on the motion of a single particle, the self-diffusion coefficient, $D_s(t)$, depends only on time and volume fraction and not on the scattering wavenumber. It equals the collective diffusion coefficient in the limit of infinite q [25]. The self-diffusion coefficient is proportional to the slope of the particle mean-squared displacement curve [20] and, for hard spheres, is given by [15,20,26]

$$D_s(t) = D_s^s - (D_s^s - D_s^l)\frac{2\sigma}{\sqrt{\pi}}\left[\frac{t}{\tau_M}\right]^{1/2} \quad \text{as} \quad t \to 0+, \tag{2}$$

and

$$D_s(t) = D_s^l + (D_s^s - D_s^l)\frac{\sigma}{2\sqrt{\pi}}\left[\frac{\tau_M}{t}\right]^{3/2} \quad \text{as} \quad t \to \infty, \tag{3}$$

where D_s^l is the long-time self-diffusion coefficient, D_s^s is the short-time self-diffusion coefficient, τ_M is the relaxation time of the velocity autocorrelation function [27], and σ is the width of the relaxation rate spectrum [26]. For dilute particle suspensions, $D_s(t) = D_0$, the characteristic time for structural rearrangements $\tau_M = \tau_0$, and $\sigma = \sqrt{2}$ [20,26]. For more concentrated suspensions such analytical relations for τ_M and σ are not available. Based on simulations Cichocki and Hinsen [26,27] suggested that $\tau_M \lesssim \tau_0$ and $\sigma \gtrsim \sqrt{2}$.

It has been reported that the time-dependent part in Eqs. (2) and (3) has a small relative amplitude, making it problematic to observe in typical light scattering experiments and even in simulations [20,22,26,27]. Therefore, we simplify the time-dependent self-diffusion coefficient into a constant short-time self-diffusion [21–24]

$$D_s(t \ll \tau_0) \approx D_s(t \to 0) = D_s^s, \tag{4}$$

and a constant long-time self-diffusion

$$D_s(t \gg \tau_0) \approx D_s(t \to \infty) = D_s^l, \tag{5}$$

for times shorter or longer with respect to τ_0, respectively. For hard-sphere particle suspensions, D_s^s can be computed numerically using Eq. (7.2) derived by Beenakker and Mazur [12,28], while
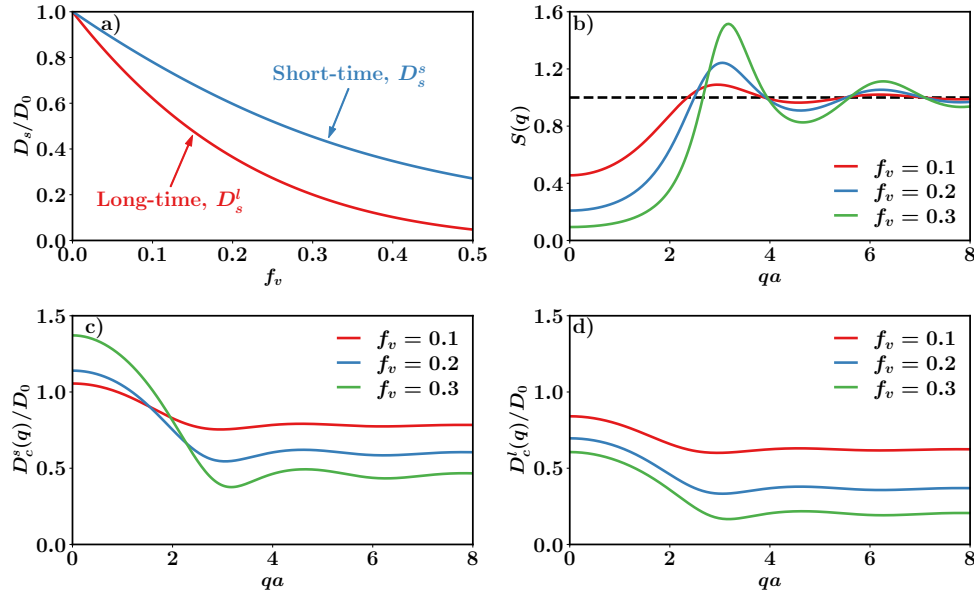
Fig. 1. Diffusion coefficients and structure factors for hard-sphere particles. (a) Self-diffusion coefficients D_s^l and D_s^s as a function of volume fraction. (b) Structure factor $S(q)$, where the dashed line corresponds to $f_v = 0$. (c) Short- and (d) long-time collective diffusion coefficients.

D_s^l can be calculated analytically using [16]

$$D_s^l = D_0 \frac{(1 - f_v)^3}{1 + 1.5 f_v + 2 f_v^2 + 3 f_v^3} . \tag{6}$$

Both D_s^s and D_s^l are plotted in Fig. 1(a) as a function of f_v. They decrease with increasing f_v, but D_s^s is consistently larger than D_s^l. It has been further suggested that D_s^l can be determined more accurately using [16,29–32]

$$D_s^l = D_0 \frac{\eta_0}{\eta}, \tag{7}$$

where η is the measured low-shear viscosity of a concentrated particle suspension.

2.1.2. Collective diffusion

Collective diffusion describes a simultaneous motion of many Brownian particles due to concentration gradients in a suspension [20]. The term "collective" refers to the coherent displacement of particles from a region of high concentration to region of low concentration [33]. In addition to dependence on t and f_v, the collective diffusion coefficient $D_c(q, t)$ also depends on the scattering wavenumber q. It has been demonstrated that the time dependency in $D_c(q, t)$ solely arises from the mean-square displacement of individual particles [11,14,34], establishing its relation to self-diffusion. Assuming uniform time-dependency across all wavenumbers, the collective diffusion coefficient can be factorized into the product of wavenumber and time-dependent factors [11,14,35], resulting in

$$D_c(q, t) = D_c^s(q) \frac{D_s(t)}{D_s^s}, \tag{8}$$

where $D_c^s(q)$ is the short-time collective diffusion coefficient given by [13]

$$D_c^s(q) = D_0 \frac{H(q)}{S(q)}, \qquad (9)$$

with $H(q)$ the hydrodynamic mobility function, and $S(q)$ the static structure factor. For hard-sphere particles, $H(q)$ can be obtained from the Beenakker-Mazur or so the called δY theory [12,13,28], and $S(q)$ can be determined using the Percus-Yevick approximation [36–38]. For dilute suspensions, i.e. for suspension for which $f_v \to 0$, $S(q) = H(q) = 1$ and $D_c(q,t) = D_0$. Figure 1(b,c) shows theoretical curves for $S(q)$ and $D_c^s(q)$, respectively, for hard-sphere particles as a function of the dimensionless wavenumber qa and f_v. At low qa values, $S(q)$ is small, reflecting the suppression of long wavelength density fluctuations in concentrated suspensions, while at large qa, it approaches unity. The short-time collective diffusion is highest at low qa and converges to D_s^s at large qa.

Since the time-dependency in collective diffusion arises from self-diffusion, we can use the same approximation as in Eq. (4), (5) and simplify $D_c(q,t)$ for shorter times into

$$D_c(q, t \ll \tau_0) \approx D_c(q, t \to 0) = D_c^s(q) = D_0 \frac{H(q)}{S(q)}, \qquad (10)$$

and for longer times into

$$D_c(q, t \gg \tau_0) \approx D_c(q, t \to \infty) = D_c^l(q) = D_0 \frac{H(q)}{S(q)} \frac{D_s^l}{D_s^s}. \qquad (11)$$

The long-time collective diffusion coefficient $D_c^l(q)$ is given in Fig. 1(d) as a function of qa and f_v. The long-time collective diffusion coefficient is consistently smaller than its short-time counterpart due to the direct electrosteric interactions that hamper particle movement; these interactions are not yet operative at short times [21].

Dynamic light scattering optical coherence tomography (DLS-OCT) can be used to measure the wavenumber-dependent collective diffusion coefficient of a particle suspensions by analyzing temporal fluctuations in the scattered light intensity for different wavenumbers detected by the OCT spectrometer. When the reference power is much larger than the sample power (at least an order of magnitude larger), DLS-OCT measures the collective diffusion coefficient using a heterodyne detection scheme [20]. When the optical properties of the particles are identical and the particles are monodisperse, all intensity fluctuations arise from microscopic density changes. The normalized autocovariance of q-dependent spectral intensity fluctuations, which is the heterodyne correlation function, is given by

$$g_1(q, \tau) = \frac{S_c(q, \tau)}{S(q)} = \frac{1}{1 + \frac{1}{\text{SNR}(q)}} e^{-D_c(q)q^2\tau} = A(q)e^{-D_c(q)q^2\tau}, \qquad (12)$$

where $\text{SNR}(q)$ is the signal-to-noise ratio as defined in [39], τ is the lag time, $A(q)$ is the autocovariance amplitude containing the effect of a diminishing SNR, $S(q, \tau)$ is the collective dynamic structure factor [20], and $D_c(q)$ is the short- or long-time collective diffusion coefficient. Here we have neglected the time dependence of the collective diffusion coefficient based on Sec. 2.1.2. Whether $D_c^s(q)$ or $D_c^l(q)$ is measured depends on the DLS-OCT acquisition time and particle size (through τ_0). Equation (12) is also known as the first-order autocorrelation function and decorrelates with a decay rate of $D_c(q)q^2$ in contrast to the scattered intensity correlation function obtained from spatially resolved OCT intensity measurements, which decays at twice this rate [5,10]. Note that the collective diffusion rate is q-dependent in contrast to the self-diffusion which is q-independent.

2.2.   Particle polydispersity

In the previous section, single-size monodisperse particles were assumed. However, particle polydispersity significantly affects the DLS-OCT correlation measurements. We distinguish between size polydispersity, particularly relevant for dilute samples, and optical polydispersity, which holds broader significance and becomes more relevant when measuring particle diffusion in concentrated suspensions.

2.2.1.   Particle size polydispersity

When particle sizes in a suspension are not identical, the sample is polydisperse in size. For large size polydispersities single exponential fits using Eq. (12) underestimate the decay rate [40]. In dilute suspensions, size polydispersity affects $g_1(q, t)$ by introducing additional higher-order correlation terms (in time) in the exponent in Eq. (12), where the magnitude of these terms is related to the degree of polydispersity [20]. For dilute particle suspensions, size polydispersity can be accounted for in the correlation function using cumulant or Laplace analysis [40]. In the cumulant analysis, instead of using D_0 in the exponent of Eq. (12), the temporal evolution of the exponent is expanded as a polynomial as proposed in [40],

$$g_1(q, \tau) = A(q)e^{-D_0 q^2 \tau + \frac{\mu_2}{2}\tau^2 - \frac{\mu_3}{3!}\tau^3 + \frac{\mu_4}{4!}\tau^4 - \cdots}, \tag{13}$$

where μ_j corresponds to the jth order in the cumulant analysis. Including the second order in τ in the expansion, the intensity-averaged polydispersity index is then defined as [2,40]

$$\text{PDI}_I = \frac{\mu_2}{\left(D_0 q^2\right)^2} = \frac{\sigma_I^2}{\langle a \rangle_I^2}, \tag{14}$$

where $\langle a \rangle_I$ and σ_I represent the mean and standard deviation (width) of the intensity-averaged particle radius distribution, respectively. The second equality hols true only for Gaussian-distributed particle sizes [41]. For perfectly monodisperse particles, $\text{PDI}_I = 0$.

When measuring diffusion of particles small compared to the wavelength of DLS-OCT, the Rayleigh scattered intensity is proportional to the squared volume of the particle [42]. In this case, the first-order autocorrelation function measures quantities averaged over the squared volume of the particle, and $\text{PDI}_I = \text{PDI}_{v^2}$. Theoretically, the measured polydispersity index may vary as a function of q due to the scattering anisotropy in DLS-OCT. However, for small particles with isotropic scattering properties this effect can be neglected [43].

2.2.2.   Optical polydispersity

Optical polydispersity refers to the variation of optical properties of the particle scattering amplitude and includes the size polydispersity [20]. Even if all particles are identical and statistically equivalent, their scattering amplitudes can vary due to non-uniform illumination intensity and light scattering directions caused by a nonzero system numerical aperture (NA). Variations in particle size, shape, and refractive index significantly increase the optical polydispersity. In an optically perfect monodisperse system, intensity fluctuations arise solely from microscopic density changes. However, optical polydispersity gives rise to variations in the scattering intensity that are not related to microscopic density changes. For example, when two optically distinct particles interchange their positions, the scattered intensity changes but the microscopic density remains unchanged [20]. This intensity fluctuation is solely related to self-diffusion. The autocovariance of these intensity fluctuations is related to the self-diffusion of these particles instead of the collective diffusion. As a result, for optically polydisperse systems, an additional self-diffusion term appears in $g_1(q, t)$. For particles with a narrow size distribution, $g_1(q, t)$ can

be approximated using the decoupling approximation [20,23,44,45]

$$g_1(q, \tau) = \underbrace{A_c(q)e^{-D_c(q)q^2\tau}}_{\text{collective term}} + \underbrace{A_s(q)e^{-D_s q^2\tau}}_{\text{self-term}}, \tag{15}$$

where $D_c(q)$ and D_s are the short- or long-time collective and self-diffusion coefficients. Higher-order terms in the exponents, similar to Eq. (13), due to the size polydispersity are neglected. The mode amplitudes $A_c(q)$ and $A_s(q)$ are the relative weights of the collective and self-diffusion terms and given by [20]

$$A_c(q) = \frac{\langle B(q)\rangle_N^2}{\left(\langle B^2(q)\rangle_N - \langle B(q)\rangle_N^2 + \langle B(q)\rangle_N^2 S(q)\right)\left(1 + \frac{1}{\text{SNR}(q)}\right)}, \tag{16}$$

and

$$A_s(q) = \frac{\langle B^2(q)\rangle_N - \langle B(q)\rangle_N^2}{\left(\langle B^2(q)\rangle_N - \langle B(q)\rangle_N^2 + \langle B(q)\rangle_N^2 S(q)\right)\left(1 + \frac{1}{\text{SNR}(q)}\right)}, \tag{17}$$

where $B(q)$ is the particle scattering amplitude and $\langle..\rangle_N$ denotes number-averaged quantities. The collective term of Eq. (15) is often called "coherent" due to a scattering contribution from coherent particle motions, while the self term is referred to as "incoherent" due to the unrelated scattering from individual particles [19,35,46]. The self and collective modes in Eq. (15) become evident only at high particle concentrations when the collective and self-diffusion coefficients are different. In dilute particle suspensions there is always only one mode because $D_c(q) = D_s = D_0$, and Eq. (15) simplifies into Eq. (12).

In suspensions where particles are made from the same material, we assume that the variation in refractive index between particles can be neglected [47]. In typical low-NA OCT systems, the beam intensity and scattering angle variations among the particles are also negligible. In this case, the optical polydispersity arises solely from the size polydispersity. If we further assume that particles are much smaller than the wavelength ($a \ll \lambda$) such that the scattering process is described by Rayleigh scattering [42,48], we find that $B(q) \propto a^3$ [49]. For particles with a number-based Gaussian size distribution, the ratio of the self and collective mode amplitudes is given by

$$\frac{A_s(q)}{A_c(q)} = \frac{\langle B^2(q)\rangle_N - \langle B(q)\rangle_N^2}{\langle B(q)\rangle_N^2} = \frac{15 \cdot \text{PDI}_N^3 + 36 \cdot \text{PDI}_N^2 + 9 \cdot \text{PDI}_N}{9 \cdot \text{PDI}_N^2 + 6 \cdot \text{PDI}_N + 1}, \tag{18}$$

where PDI_N is the particle number-based polydispersity index defined as

$$\text{PDI}_N = \frac{\sigma_N^2}{\langle a\rangle_N^2}, \tag{19}$$

with $\langle a\rangle_N$ and σ_N being the mean and the standard deviation (width) of the number-averaged particle radius distribution. The ratio of the self and collective mode amplitudes contains information about the sample's number polydispersity. As expected, the self mode vanishes for a perfectly monodisperse particle suspension ($\text{PDI}_N = 0$), resulting in the simplification of Eq. (15) into Eq. (12).

Figure 2(a) shows simulated volume-based and intensity-based polydispersity indices (PDI_v and PDI_I, respectively) for particles characterized by a Gaussian number-based size distribution with a number polydispersity index PDI_N. For the considered PDI_N values, both volume-based and intensity-based distributions exhibit a Gaussian shape. Up to $\text{PDI}_N = 0.02$, all three
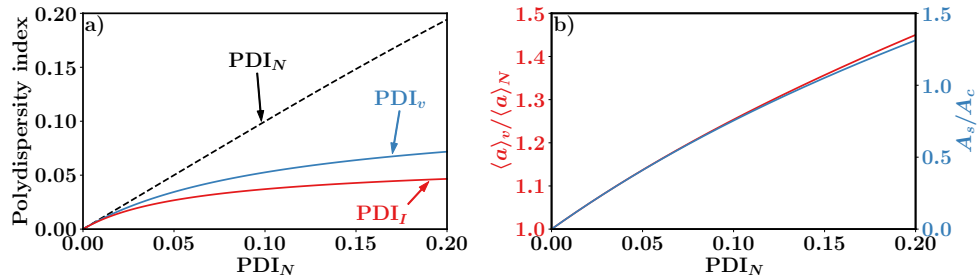
Fig. 2. Simulated Gaussian number-based particle size distribution: (a) comparison of number, volume, and intensity-based polydispersity indices. (b) Ratios $\frac{\langle a \rangle_v}{\langle a \rangle_N}$ and $\frac{A_s}{A_c}$ as functions of PDI_N.

polydispersity indices are similar. PDI_v and PDI_I remain close even up to $\text{PDI}_N = 0.04$, but they start to deviate for larger PDI_N values.

In Fig. 2(b), it is illustrated that the quantity $\frac{\langle a \rangle_v}{\langle a \rangle_N}$, the ratio of volume- to number-averaged particle radii, is nearly proportional to PDI_N, serving as a good indicator for the number-based polydispersity index. For a number-based Gaussian size distribution, the relationship is given by

$$\frac{\langle a \rangle_v}{\langle a \rangle_N} = \frac{3 \cdot \text{PDI}_N^2 + 6 \cdot \text{PDI}_N + 1}{3 \cdot \text{PDI}_N + 1}. \tag{20}$$

Furthermore, in Fig. 2(b), we can observe how the ratio of the self and collective modes increases with higher PDI_N. At $\text{PDI}_N = 0.14$, which corresponds to a PDI_I of approximately 0.04 for a Gaussian number distribution, the self and collective terms become equal. Consequently, for samples with much larger PDI_I, we anticipate A_s from Eq. (15) to be significantly larger than A_c.

3. Methods

3.1. OCT systems

Dynamic light scattering experiments were performed using two OCT systems. A custom-built relatively slow ultra-broadband OCT system and a fast relatively narrowband Thorlabs GANYMEDE II HR series spectral domain OCT. The latter, based on a stable superluminescent diode, has been described in detail in our previous work [10,39]. Both OCT systems have a backscattering configuration with NA = 0.05 and were operated in M-scan mode where subsequent A-scans were acquired at a fixed sample position. All measurements were performed at room temperature. Table 1 summarizes important parameters for both OCT systems. Figure 3(a) shows the layout of our custom setup.
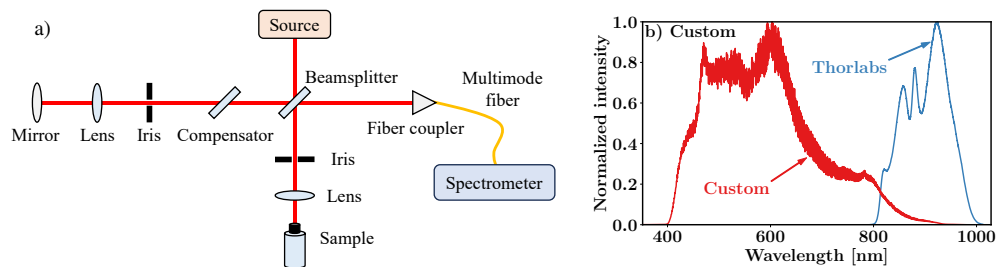

Fig. 3. (a) Schematic overview of the custom-made OCT system. (b) DC spectra of the custom-built and Thorlabs OCT system.

Table 1. System parameters for the custom-built and Thorlabs OCT setup.

Setup	k_0 range [μm^{-1}]	FWHM$_\lambda$ [nm]	FWHM$_z$ [μm]	z_{max} [mm]	Rate [kHz]
Custom	$6.49 - 15.64$	217	0.6	0.27	4.5
Thorlabs	$6.23 - 7.82$	112	3.1	1.87	36.0

The custom spectral-domain OCT setup was built using a supercontinuum laser from NKT Photonics with an emission spectrum from visible to mid-infrared range. Data was acquired with a high-speed spectrometer (Ocean FX, Ocean Optics) covering a wavelength range of $350 - 1000$ nm. The optics was designed for the same wavelength range, utilizing achromatic lenses (AC254-050-AB-ML, $f = 50$ mm, Thorlabs), a plate beamsplitter (BSW26R, Thorlabs), a beamsplitter compensator (BCP42R, Thorlabs), and silver mirrors (PF10-03-P01, Thorlabs). Backscattered sample and reference beams were coupled into a multi-mode fiber connected to the spectrometer. Since the coherence length and NA are very low, the optical variation in q due to a varying scattering angle is much smaller than the variation in q due to spectral sampling in k_0. Therefore, it can be assumed that the scattering angle is 180° and the scattering wavenumber q in the correlation analysis is $q = 2nk_0$.

Reference spectra of both OCT systems are shown in Fig. 3(b). The custom-built setup has a lower temporal sampling rate but much larger wavelength range than the Thorlabs OCT system. The custom-built setup has a higher noise level due to several reasons. First, the supercontinuum source has a higher noise floor and worse sensitivity roll-off characteristics [50] compared to the superluminescent diode used in the Thorlabs system. Second, the custom setup uses a multimode fiber to deliver the interfered light to the spectrometer whereas the Thorlabs system is solely based on single-mode fibers. The interference between different fiber modes increases the noise level. It was not possible to use the single-mode fiber with our custom setup due to the single-mode fiber's limited spectral transmission bandwidth.

3.2. Particle suspensions

Four concentrated and NaCl charge-stabilized aqueous silica suspensions were procured. The manufacturer-provided silica mass fraction in each sample was 50 wt.%. All relevant manufacturer-provided sample properties are summarized in Table 2. Particle surface (Zeta) potential measurements were not provided; they were obtained separately, along with transmission electron microscope (TEM) images. The obtained TEM images are shown in Fig. 9 in the Appendix. The measured Zeta potentials are strongly negative, indicating that the suspensions are very stable against coalescence [51].

For the Kostrosöl samples manufactured and supplied by Chemiewerk Bad Köstritz GmbH (CWK), the particle size distribution (PSD) properties were determined by the manufacturer using a CPS Disc Centrifuge (CPS Instruments, USA), and they are provided in the Appendix. Both volume and number-averaged distributions are depicted. The volume-based PSDs for all samples exhibit a single peak around the mean particle size, resembling normal or log-normal size distributions. In the case of Kostrosöl 9550, the number-based PSD is similar. However, in

Table 2. Manufacturer provided and measured sample properties.

Sample	$\langle a \rangle_v$ [nm]	PDI$_v$	$\frac{\langle a \rangle_v}{\langle a \rangle_N}$	Zeta [mV]	η [cP]
Kostrosöl 8050	38.2	0.027	1.645	-43.3 ± 2.4	5.9
Kostrosöl 9550	37.5	0.033	1.033	-36.7 ± 2.8	6.0
Kostrosöl 10050	49.7	0.018	1.195	-45.1 ± 0.8	4.7
Levasil CS50-28	-	-	-	-51.7 ± 0.7	-

Kostrosöl 8050 and 10050, additional peaks in the number-based PSDs are observed due to the presence of a large number of smaller particles. While these smaller particles scatter almost no light and are negligible in the volume-averaged scheme, they are significant in the number-based PSD.

Levasil CS50-28, manufactured by Nouryon and supplied by Inprocess-LSP, was provided to us as a more polydisperse sample with a particle radius range of 5-75 nm. However, detailed information about the particle properties is not available. DLS measurements from literature report an average particle radius of 55 nm [52]. However, it's important to note that this value may vary from batch to batch.

In Table 2, $\langle a \rangle_v$ is the mean radius, and PDI_v denotes the polydispersity index of the volume-based particle radius distribution measured by the manufacturer. Since the exact shapes of the distributions in the Appendix are unavailable to us, the volume-based polydispersity index was approximated by dividing the square of the full width at half maximum ($FWHM_v$) by the square of the mean radius. The quantity $\frac{\langle a \rangle_v}{\langle a \rangle_N}$, as provided by the manufacturer and shown in Fig. 10 in the Appendix, represents the ratio of volume-averaged to number-averaged particle radius. As illustrated in Fig. 2(b), this ratio is directly related to the number-based polydispersity in Eq. (19).

The particle volume fraction f_v is necessary for calculating the theoretical collective and self-diffusion coefficients. Even though our particles are charge-stabilized, we did not know the exact thickness of the electric double layer around them, which can significantly affect f_v [16]. For that reason we diluted our original suspensions with a small amount of highly concentrated LiCl solution (mixing ratio 110:1). This did not affect the silica weight content when rounded to the nearest integer but resulted in approximately 14 mM LiCl concentration in the suspensions. At this salt concentration the thickness of the electrical double layer can be neglected and the particles can be treated as hard-spheres [16,53]. To determine f_v we have used the simplest approach based on the particle mass and density [54] with

$$f_v = \left[1 + \frac{\rho_s}{\rho_w} (w_s^{-1} - 1) \right]^{-1}, \tag{21}$$

where w_s is the manufacturer stated silica mass fraction in the suspension, $\rho_s \approx 2.0$ g/mL and $\rho_w = 1.0$ g/mL are the silica particle and water densities [55], respectively. Based on Eq. (21) and $w_s = 0.5$, and for all provided samples the maximum volume fraction is $f_v \approx 0.33$.

The mean sample refractive index n was calculated by finding the refractive indices of water and silica separately and then mixing them using the Lorentz-Lorenz formula [56,57]. The refractive index of water as a function of wavelength and temperature was calculated using [58], and the refractive index of silica at the room temperature as a function of wavelength was estimated using [59]. Since all suspensions have the same f_v, we assume that their refractive indices are identical.

3.3. Diffusion measurements in dilute suspensions

Dilute suspensions were prepared using the demineralized water with a silica weight content of 1 wt.% corresponding to $f_v \approx 0.005$. This is sufficiently low to neglect particle interactions and multiple scattering. The LiCl concentration was maintained at the same level as in dense suspensions. In dilute suspensions D_0 is constant and does not depend on q. Therefore, all DLS-OCT measurements were performed in the depth-domain using the Ganymede OCT system. The dilute suspensions were used to determine D_0 and PDI_I for all samples. In order to convert D_0 to the particle hydrodynamic radius, the viscosity of the dilute aqueous solution, η_0, was calculated using Eq. (21) from [60].

Every OCT acquisition consisted of 20 subsequent M-scans, each containing 32768 temporal sampling points. The measured interference spectrum was first resampled to a linearly-sampled wavenumber domain and then apodized using a Gaussian filter. After apodization, the measured

FWHM$_z$ was 4.67 µm, exceeding the unapodized FWHM$_z$ value in Table 1. From the complex OCT data the average of 20 first-order normalized autocorrelation functions was calculated at every depth. The depth-resolved $g_1(z, \tau)$ was noise-corrected [61,62] and averaged over the depth range with SNR>10 inside the sample. The resultant average $g_1(\tau)$ was fitted using Eq. (13) with $A = 1/(1 + \text{SNR}^{-1})$, $D_c = D_0$, and μ_j as free parameters. The second- or fourth-order nonlinear fits were performed depending on the sample polydispersity [40] for the range of τ for which $g_1(\tau)>0.01$. The intensity-averaged particle size and PDI$_I$ were subsequently calculated using Eq. (1) and Eq. (14).

3.4. Diffusion measurements in concentrated suspensions

Wavenumber-domain DLS-OCT measurements were performed either with the custom or Thorlabs OCT system. Due to temporal sampling and sensitivity limitations, only the samples with the largest particles, Kostrosöl 10050 and Levasil CS50-28, could be measured using the custom setup. The small particles, Kostrosöl 8050 and 9550, were measured using the Thorlabs system. Two additional suspensions were made by mixing both samples in each pair with 1:1 mixing ratio. In total 20 measurements were performed with 8192 and 32768 temporal sampling points for the custom and Thorlabs systems, respectively.

Wavenumber-dependent DLS-OCT data processing steps are shown in Fig. 4. Similar to the dilute case, we initially obtain the complex OCT signal from the spectral interference. Then we compute the average depth-resolved $g_1(z, \tau)$ and determine its decay rate as a function of depth. We identify the depth region with a constant diffusion coefficient and without the effects of multiple scattering or sensitivity roll-off [63]. We apodize the complex OCT signal in this region using the Tukey window function and transform it back to the wavenumber-domain via the forward Fourier transformation. As a result we obtain a fully real-valued spectral interference signal. Subsequently, the average temporal autocovariances are computed and fitted for every k_0 to determine the wavenumber-dependent diffusion coefficient.
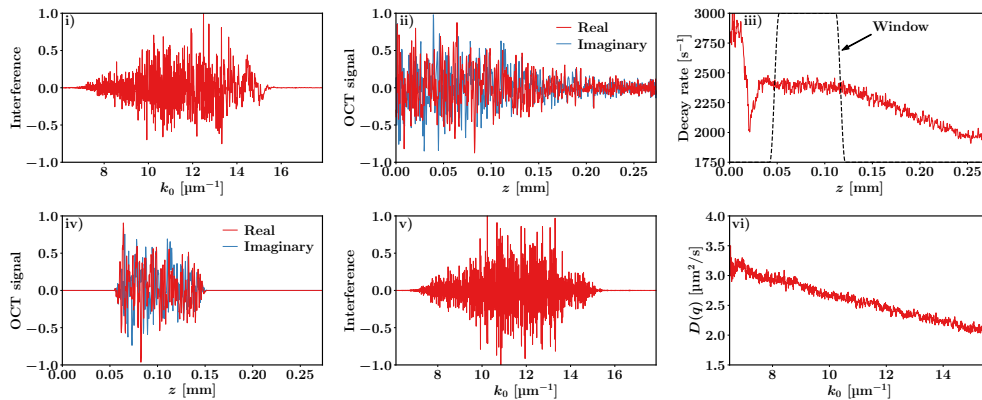

Fig. 4. Overview of the processing steps in DLS-OCT for obtaining the wavenumber-dependent diffusion coefficient in a single acquisition. The data are from the custom-built setup where we measured the collective diffusion coefficient in the Kostrosöl 10050 sample, containing 100 nm particles at $f_v = 0.33$.

In concentrated suspensions, particle size polydispersity can affect both the collective [20,24] and self-diffusion [64,65] coefficients. For purely exponential decays Eq. (12) is used to fit with autocovariance amplitude and the diffusion coefficient as fit parameters. For $g_1(q, \tau)$ with a non-exponential behaviour we use Eq. (15) to fit with A_c, A_s, D_c, and D_s as fit parameters.

4. Results

Table 3 presents the results obtained from dilute particle suspensions using the Thorlabs OCT system. Diffusion coefficients were obtained by fitting Eq. (13), and particle radii were determined using the Stokes-Einstein relation. The errors in radii were calculated by propagating the assumed temperature uncertainty of half a degree and incorporating statistical errors. Polydispersity indices were then calculated using Eq. (14). Interaction times, calculated using $\tau_0 = \langle a \rangle_I^2 / D_0$, are also given. In general, the intensity-averaged particle sizes and PDI_I align well with the volume-averaged values provided by the manufacturer in Table 2. The measured PDI_I values for Kostrosöl samples are comparable in magnitude and slightly lower than the corresponding PDI_v from the manufacturer. This observation is consistent with our expectations for relatively monodisperse samples, as indicated in Fig. 2. In contrast to Kostrosöl samples, Levasil CS50-28 and its mixtures exhibit significantly higher levels of polydispersity.

Table 3. Measured parameters for dilute particle suspensions using the Thorlabs OCT system.

Sample	$\langle a \rangle_I$ [nm]	PDI_I	τ_0 [ms]
Kostrosöl 8050	38.9 ± 1.1	0.022 ± 0.002	0.26
Kostrosöl 9550	37.4 ± 1.1	0.022 ± 0.002	0.23
Kostrosöl 8050 & 9550 1:1 mix	38.6 ± 1.2	0.023 ± 0.002	0.26
Kostrosöl 10050	48.6 ± 1.5	0.018 ± 0.002	0.51
Levasil CS50-28	51.7 ± 1.6	0.162 ± 0.003	0.62
Levasil CS50-28 & Kostrosöl 10050 1:1 mix	49.9 ± 1.6	0.101 ± 0.004	0.56

4.1. Kostrosöl 10050 and Levasil CS50-28 measurements

Autocorrelation functions for dilute (depth-domain, Thorlabs OCT) Levasil CS50-28, Kostrosöl 10050, and their mixture are shown in Fig. 5(a). As expected from Eq. (13), the autocorrelation function of dilute samples deviates from the single exponential trend with increasing size polydispersity. Autocorrelation functions for concentrated (q-domain, custom OCT) Levasil CS50-28, Kostrosöl 10050, and their mixture are shown in Fig. 5(b). The concentrated suspensions do not exhibit a double exponential decay; instead, we observe only a single term from Eq. (15). We attribute this to a combination of factors, such as low sensitivity and low acquisition rate of the custom setup, very high or very low sample polydispersity, used qa range, and differences in decay rates between the collective and self-terms at longer time scales. Hence, a single exponential function was employed to fit the wavenumber-dependent diffusion coefficient $D(q)$.

The concentrated samples are analyzed in the q-domain with the custom setup which operates with an acquisition time $\Delta t = 222$ ms. This implies that we are in the long-time diffusion regime, with $\tau \gg \tau_0$ for all particles. The obtained wavenumber-dependent diffusion coefficients for concentrated suspensions with $f_v \approx 0.33$ are given in Fig. 6. For comparison, the theoretical D_s^l and $D_c^l(q)$ from Sec. 2.1.1 and 2.1.2 are also shown. These were calculated with hard-sphere models presented in Sec. 2 and a volume fraction of 0.33 and the particle radii from Table 3. For Kostrosöl 10050, D_s^l was estimated based on the provided sample viscosity and using Eq. (7). The viscosity for Levasil CS50-28 was not known, so D_s^l was calculated using Eq. (6). The obtained diffusion coefficients were normalized using D_0 values of the diluted suspensions, corresponding to the radii in Table 3. The measured $D(q)/D_0$ for Kostrosöl 10050 is wavenumber-dependent and agrees remarkably well with the long-time collective diffusion coefficient. For Levasil CS50-28 the obtained $D(q)/D_0$ is constant and matches well to the long-time self-diffusion coefficient. For the mixed sample $D(q)$ is also constant (marginally q-dependent) and lies in between D_s^l and

$D_c^l(q)$. At the edges of the spectrum the obtained diffusion coefficient fluctuates, which is caused by a reduction in the signal-to-noise ratio at these wavenumbers.
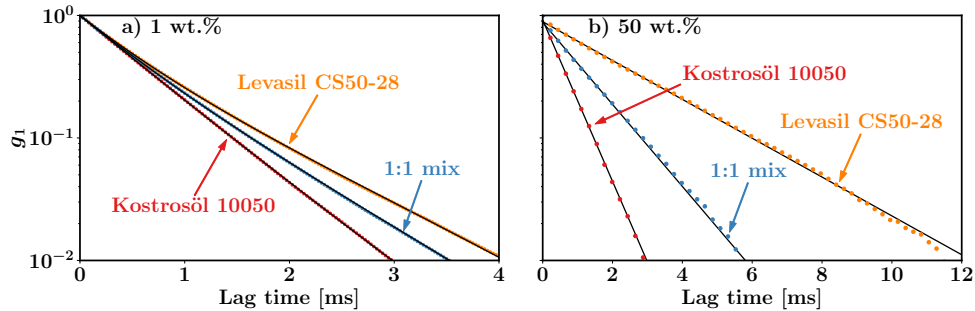

Fig. 5. Autocorrelation function of Levasil CS50-28, Kostrosöl 10050, and their mixture. (a) Depth-averaged $g_1(\tau)$ obtained at the center wavenumber $q_c = 18.8\ \mu m^{-1}$ in dilute suspensions using the Thorlabs OCT, fitted with Eq. (13). (b) Wavenumber-dependent $g_1(q, \tau)$ measured in concentrated samples for $q = 22.7\ \mu m^{-1}$ using the custom OCT system, fitted with Eq. (12). Black solid lines represent the fits.
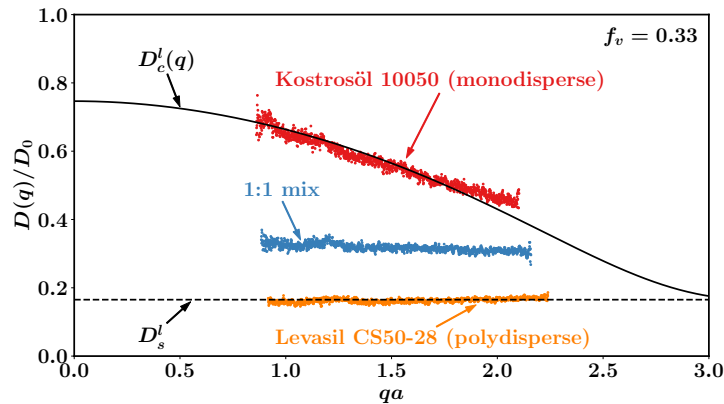

Fig. 6. Measured q-dependent diffusion coefficient for Levasil CS50-28 (polydisperse), Kostrosöl 10050 (monodisperse), and their mixture at $f_v = 0.33$.

4.2. Kostrosöl 8050 and 9550 measurements

The short-time dynamics of concentrated Kostrosöl 8050 and 9550 samples are shown in Fig. 7(a-i). All measurements were performed using the Thorlabs OCT system with a much higher acquisition rate and lower noise compared to the custom setup. In this case, $\Delta t = 0.028 \ll \tau_0$ ms, which implies that we are in the short-time diffusion regime. The double-exponential behavior in concentrated samples was clearly visible, which is why we used Eq. (15) to fit the collective and self-diffusion coefficients. Figure 7(a,b,c) show the obtained first-order normalized autocovariance functions both for dilute and concentrated suspensions. The correlation functions are very similar because all samples are quite monodisperse and have similar particle sizes and concentrations. For the same reason we see in Fig. 7(d,e,f) that the measured $D_c(q)$ and D_s from all samples are almost identical. In this case, $D_c(q)$ matches well with the short-time collective diffusion coefficient from Eq. (9), and D_s matches the short-time self-diffusion coefficient from
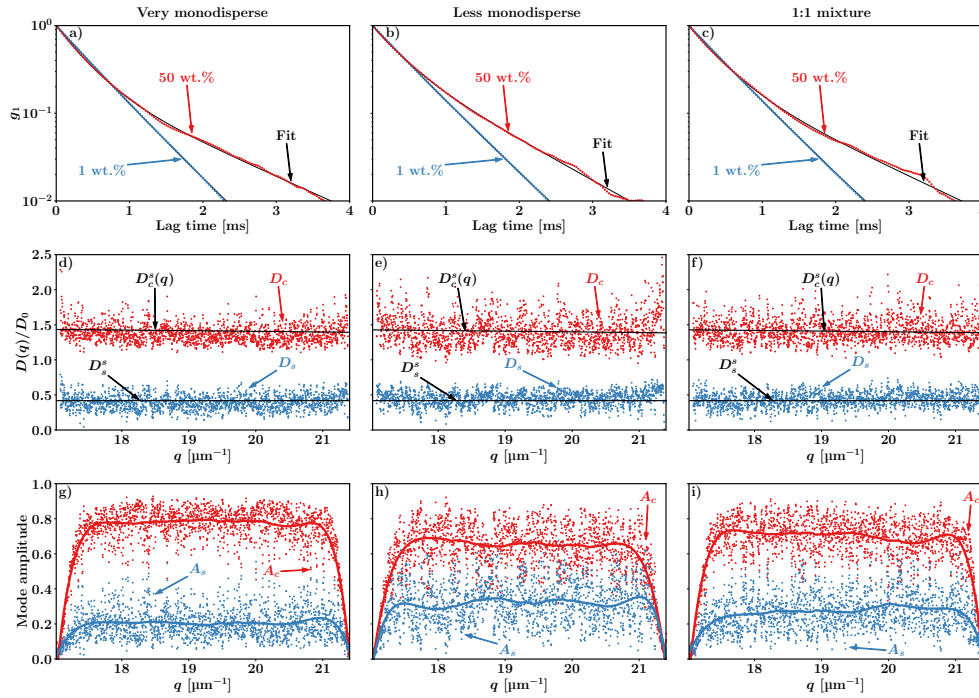
Fig. 7. Kostrosöl 9550 (very monodisperse) and 8050 (less monodisperse), and their mixture. (a-c) Measured and fitted $g_1(q = 18.8\,\mu m^{-1}, \tau)$. (d-f) Measured and theoretical collective and self-diffusion coefficients. (g-i) Measured and smoothed collective and self mode amplitudes obtained using Thorlabs OCT.

Eq. (4). The presence of noise is also evident, highlighting the added value of averaging over different wavenumbers.

Since the self-term becomes visible at larger lag times, it is theoretically possible that we measure D_s^l rather than D_s^s. However, the obtained results match well with the calculated values of D_s^s. The only parameters that differ among these samples are the mode amplitudes $A_c(q)$ and $A_s(q)$, as shown in Fig. 7(g,h,i). Here, the solid curves correspond to wavenumber-smoothed data. We see that $A_c(q)$ is highest for Kostrosöl 9550 and lowest for Kostrosöl 8050, while $A_s(q)$ is highest for Kostrosöl 8050 and lowest for Kostrosöl 9550. These differences can be explained by the difference in size polydispersities between these samples. Despite having nearly identical volume-based and intensity-based polydispersity indices, the number-based particle size distribution for Kostrosöl 8050 exhibits significantly less monodispersity, as shown in Fig. 10(b), compared to that of Kostrosöl 9550, as illustrated in Fig. 10(d). Hence, the self-diffusion amplitude for Kostrosöl 8050 is larger. This contrast is highlighted by the provided $\frac{\langle a \rangle_V}{\langle a \rangle_N}$ data from Table 2.

Particle number-based polydispersity indices were calculated from measurements of concentrated samples using the ratio of collective and self-mode amplitudes. This approach is valid at all diffusion time scales. For each sample we calculated $\frac{A_s(q)}{A_c(q)}$ and averaged it over the wavenumber range with SNR>10. PDI$_N$ values were determined numerically by inverting Eq. (18) and the results are given in Table 4. Unlike the intensity-based polydispersity indices measured in dilute samples, the PDI$_N$ obtained from concentrated suspensions differs between Kostrosöl samples indicating the variation in number polydispersity. While PDI$_N$ is not directly comparable with

the manufacturer-provided $\frac{\langle a \rangle_v}{\langle a \rangle_N}$ from the Appendix, we expect them to be almost proportional based on Fig. 2(b), which is exactly what we observe in Table 4.

Table 4. PDI$_N$ obtained from concentrated particle suspensions using Thorlabs OCT, along with the manufacturer-provided ratio $\frac{\langle a \rangle_v}{\langle a \rangle_N}$.

Sample	PDI$_N$	$\frac{\langle a \rangle_v}{\langle a \rangle_N}$
Kostrosöl 8050	0.061 ± 0.002	1.645
Kostrosöl 9550	0.029 ± 0.001	1.033
Kostrosöl 8050 & 9550 1:1 mix	0.045 ± 0.001	1.379

5. Discussion

In this work we investigated q-dependent diffusion coefficients in concentrated (silica) particle suspensions at short and long times. We measured collective and/or self-diffusion coefficients in samples with similar particle sizes and varying degrees of size (and optical) polydispersities. The results were consistent with calculations based on hard-sphere diffusion theory.

We determined the long-time diffusion coefficients in Levasil CS50-28 and Kostrosöl 10050 samples using a custom-built OCT system with a broad wavelength range and a relatively long sampling time. The average particle size for both samples was nearly 100 nm, but the polydispersities were different. In monodisperse Kostrosöl 10050 we measured the wavenumber-dependent collective diffusion coefficient $D_c^l(q)$. The obtained $g_1(q, \tau)$ was pure single exponential and the self-diffusion term from the decoupling approximation could not be observed. This is primarily attributed to low size and optical polydispersities of the sample. The sample Levasil CS50-28 exhibited much greater polydispersity; however, in this case, only the self-diffusion coefficient D_s^l was measured. This suggests that, in this scenario, the self-diffusion contribution to the correlation function is significantly larger compared to the collective diffusion. This is precisely what we expect when we analyze the curves in Fig. 2(a,b). Here, we anticipate that the PDI$_N$ values of Levasil CS50-28 and its mixture will be very high, resulting in $A_s \gg A_c$. Therefore, it is unsurprising that only self-diffusion is measured, which also is in good agreement with the theoretical estimate. The diffusion coefficient obtained from the mixed sample remained nearly constant with q and was notably higher than D_s^l. Due to the high sample polydispersity, it is more likely that we are still measuring self-diffusion, but D_s^l deviates from the value predicted by Eq. (6). Therefore, similar to the method used for Kostrosöl 10050, a viscosity measurement is needed to estimate D_s^l more accurately using Eq. (7). Additionally, there is a possibility that both the collective and self terms were measured, but they cannot be separated. It has been suggested that when the amplitudes and the diffusion coefficients of the collective and self-diffusion modes are comparable, separating these modes becomes problematic, resulting in the measurement of a mixed diffusion coefficient [17]. Overall, the decoupling approximation appears to work remarkably well even for moderately polydisperse samples.

We employed the fast acquisition Thorlabs OCT system to measure the short-time diffusive dynamics in Kostrosöl 8050 and 9550. These suspensions were quite monodisperse with the average particle size of approximately 75 nm. In this case, the obtained $g_1(q, \tau)$ clearly exhibited a double-exponential behavior, enabling us to measure both the self and collective terms. This is likely attributed to the utilization of a faster and more sensitive OCT system with lower q and the use of smaller particles, resulting in lower qa value. First, as illustrated in Fig. 1(c,d), decreasing qa increases the difference between $D_c^s(q)$ and D_s^s, making the collective and self modes more distinguishable. Second, at low qa values, self-diffusion becomes significant even for monodisperse suspensions due to a reduction in the structure factor [22]. For the Thorlabs

system the wavenumber range was limited due to a narrow spectral bandwidth. Therefore, we could not clearly observe the wavenumber-dependent variations in the collective diffusion coefficient. Nevertheless, we find it feasible to measure self-diffusion even in monodisperse particle suspensions due to optical polydispersity. In this study, our primary focus was on investigating the impact of particle size variations on optical polydispersity. We did not consider refractive index dispersity, which is always present to some degree, and further contributes to increasing optical polydispersity [47].

The smallest particle radius that our custom-built DLS-OCT system can reliably measure in a dilute aqueous suspension at all wavelengths is limited by the acquisition rate of the spectrometer to around 50 nm. Additionally, the signal-to-noise ratio is constrained by the 212 µs dead time of the spectrometer. Therefore, a faster spectrometer without dead time will provide increased sensitivity and access to shorter diffusion times. Furthermore, self-interference inside the multimode fiber also decreases the experimental SNR, which could potentially be improved by altering the setup to a free-space system.

5.1. Particle sizing

Diffusion measurements can be used for in-line particle sizing during process control [66]. However, in concentrated particle suspensions there is no simple relation between the diffusion coefficient and the particle size. The self-diffusion coefficient is wavenumber-independent and depends both on particle size and concentration. So, without a-priori knowledge of the particle concentration, D_s cannot be used to determine the particle size. The collective diffusion coefficient, on the other hand, is wavenumber-dependent. So, when measured over a sufficient q-range, $D_c(q)$ can be used to determine both the particle size and concentration. This is only possible with large-bandwidth OCT systems covering a wide q-range, capable of capturing q-dependent variations in the collective diffusion coefficient.

For our long-time analysis, we inverted Eq. (11) and performed a fit for both a and f_v using the measured $D_c^l(q)$ in Kostrosöl 10050. The fitted values for particle size and volume fraction were $a = 50 \pm 2$ nm and $f_v = 0.18 \pm 0.02$, respectively. The measured and fitted $D_c^l(q)$ are shown in Fig. 8(a). The obtained particle radius is remarkably close to the expected value, but the volume fraction deviates considerably. This deviation is likely caused by an inaccurate estimation of the long-time self-diffusion coefficient using Eq. (6) in the fitting procedure. For Kostrosöl 10050, based on Eq. (7) and the measured viscosity, $D_s^l/D_0 = 0.21$. In contrast, according to Eq. (6), $D_s^l/D_0 = 0.17$. It is evident that Eq. (6) slightly underestimates D_s^l for Kostrosöl 10050. Since $D_c^l(q) \propto D_s^l$, using Eq. (6) in our fit introduces a bias into the obtained parameters. However, this bias affects f_v more because it is more sensitive to the magnitude of $D_c^l(q)$. Conversely, the particle radius is more sensitive to the slope and shape of the $D_c^l(q)$ curve, leading to a more accurate estimation.

In the short-time analysis, both the collective and self-diffusion coefficients are obtained from the fit and wavenumber-dependent measurements are not necessary to simultaneously determine
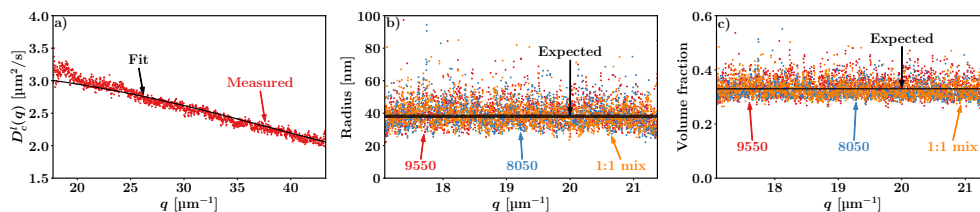

Fig. 8. (a) Measured and fitted $D_c^l(q)$ for Kostrosöl 10050. (b) Fitted particle size and (c) volume fraction for Kostrosöl 8050, 9550, and their mixture.

the values of a and f_v. In this scenario, we have two measurements of D_s^s and D_c^s and two unknown parameters, which can be solved using a nonlinear system of equations. Consequently, we inverted $D_c^s(q)$ and D_s^s from the δY theory and utilized our measurements of the samples Kostrosöl 8050, 9550, and their mixture to determine the particle radius and volume fraction in each sample. In this case, we obtain values for a and f_v at every single q without the need to fit over the large q-range. This also allows the analysis to be conducted in the depth-domain. Figure 8(b) shows the fitted a as a function of q along with the expected particle radius range for these samples. The average particle sizes over the entire q-range, along with their corresponding standard deviations, for Kostrosöl 8050, 9550, and their mixture were 39 ± 9, 41 ± 9, and 39 ± 8 nm, respectively. The averaged volume fractions obtained for these samples are presented in Fig. 8(c) and correspond to 0.32 ± 0.03, 0.34 ± 0.04, and 0.33 ± 0.04, respectively. So there is a good agreement with the expected values for a and f_v, although the noise in Fig. 8(b,c) is also significant. So, even if q-dependent measurements are not available, it is possible to obtain the particle size and volume fraction in concentrated suspensions from fast correlation measurements of both the collective and self-diffusion coefficients. Regardless of which diffusion coefficient is obtained, it is always necessary to determine whether the measurement corresponds to long- or short-time particle dynamics. This determination is not trivial, as it depends not only on the acquisition speed but also on the to-be-estimated particle size. Furthermore, accurate estimates of collective and self-diffusion, crucial in determining particle size, depend on known particle interactions. While we assumed hard-sphere interactions, in industrial scenarios, these interactions may remain unknown.

5.2. Polydispersity measurement

We observed that the intensity-based polydispersity index, PDI_I, measured using DLS-OCT in dilute particle suspensions, demonstrates less sensitivity towards smaller particles compared to its number-based counterpart, PDI_N. This difference arises from the influence of particle size on the measured PDI_I, which depends on both the scattering intensities and decay rates of the particles. Smaller particles scatter less light and exhibit faster decaying autocorrelations, making them more challenging to detect.

The PDI_I values obtained from the dilute samples Kostrosöl 8050, 9550 and their mixture using the cumulant analysis were virtually identical even though the actual number-based polydispersities were knowingly different. In concentrated suspensions, where both collective and self-diffusion are measured, we used the ratio of the self over collective mode amplitudes to determine PDI_N. Our method measures PDI_N by observing exchange diffusion, where particles swap positions, leading to variations in the intensity of scattered light. This method proved to be much more sensitive to particles of all sizes and can effectively differentiate samples with very similar PDI_v and PDI_I but different PDI_N. The results obtained using this technique closely matched our expectations based on the manufacturer-provided number polydispersities. Our approach relies on assuming a normal distribution for the particle size to establish an analytic relationship between PDI_N and $\frac{A_s(q)}{A_c(q)}$. However, our method is not restricted to Gaussian distributions and can be extended to particle size distributions of any a priori assumed shape, as long as the decoupling approximation remains valid.

6. Conclusion

We demonstrated the application of q-dependent DLS-OCT to measure both collective and self-diffusion coefficients in concentrated silica suspensions. Depending on the sample polydispersity, we successfully measured either long-time collective or long-time self-diffusion over a broad q-range using our custom-built OCT system. The obtained long-time collective diffusion coefficient agreed well with hard-sphere theory, providing further evidence for the dynamic scaling property [14]. Fitting the particle size and volume fraction of the suspension to the q-dependent collective

diffusion coefficient resulted in excellent agreement for particle size but yielded a less accurate estimate of the volume fraction.

We found the decoupling approximation to be highly effective in describing the first-order normalized autocovariance functions in both monodisperse and relatively polydisperse samples. Utilizing a high-speed yet narrow q-range Thorlabs OCT system, we simultaneously measured collective and self-diffusion even in sufficiently monodisperse samples. Using both terms allowed us to determine particle size and volume fraction at a single wavenumber. Furthermore, for a normal particle size distribution, we derived a relationship between the particle number-based polydispersity index and the ratio of the self and collective mode amplitudes. This relationship was employed to determine the size polydispersity of concentrated suspensions. Our method exhibits considerably greater sensitivity to all particle sizes compared to the standard intensity-based cumulant analysis performed in DLS on dilute samples.
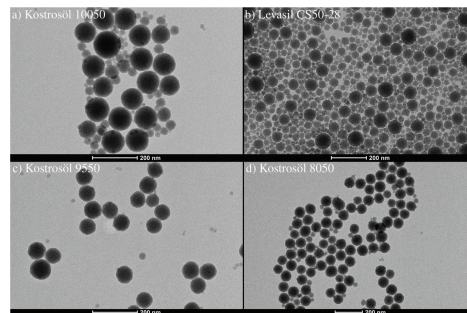
Appendix

Fig. 9. TEM images of (a) Kostrosöl 10050, (b) Levasil CS50-28, (c) Kostrosöl 9550, and (d) Kostrosöl 8050.
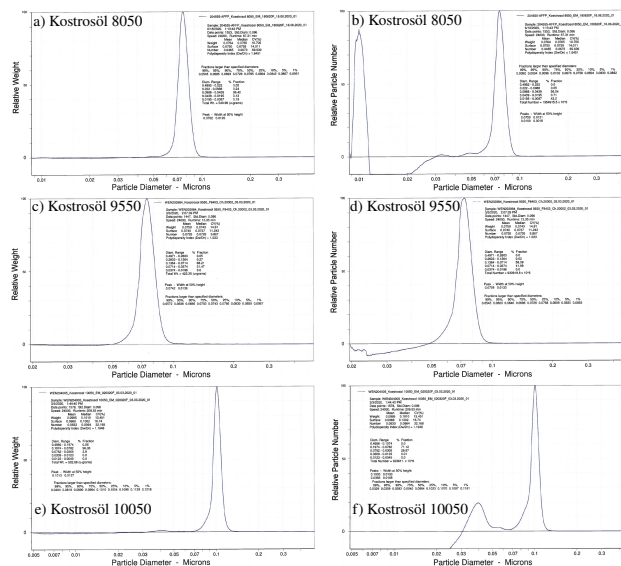

Fig. 10. Volume (left column) and number-based (right column) PSDs for Kostrosöl (a,b) 8050, (c,d) 9550, and (e,f) 10050, determined by disc centrifuge.

References

1. C. Holt, T. G. Parker, and D. G. Dalgleish, "Measurement of particle sizes by elastic and quasi-elastic light scattering," Adv. Colloid Interface Sci. **52**, 79–143 (1994).
2. W. Tscharnuter, "Photon correlation spectroscopy in particle sizing," in *Encyclopedia of Analytical Chemistry*, R. Meyers, ed. (John Wiley & Sons Ltd, Chichester, 2000), p. 5469–5485.
3. V. A. Martinez, J. H. J. Thijssen, F. Zontone, *et al.*, "Dynamics of hard sphere suspensions using dynamic light scattering and x-ray photon correlation spectroscopy: Dynamics and scaling of the intermediate scattering function," J. Chem. Phys. **134**(5), 054505 (2011).
4. A. Wax, C. Yang, R. Dasari, *et al.*, "Path-length-resolved dynamic light scattering: modeling the transition from single to diffusive scattering," Appl. Opt. **40**(24), 4222 (2001).
5. J. Kalkman, R. Sprik, and T. G. van Leeuwen, "Path-length-resolved diffusive particle dynamics in spectral-domain optical coherence tomography," Phys. Rev. Lett. **105**(19), 198302 (2010).
6. K. K. Bizheva, A. M. Siegel, and D. A. Boas, "Path-length-resolved dynamic light scattering in highly scattering random media: The transition to diffusing wave spectroscopy," Phys. Rev. E **58**(6), 7664–7667 (1998).
7. D. A. Boas, K. K. Bizheva, and A. M. Siegel, "Using dynamic low-coherence interferometry to image brownian motion within highly scattering media," Opt. Lett. **23**(5), 319–321 (1998).
8. N. Weiss, T. G. van Leeuwen, and J. Kalkman, "Localized measurement of longitudinal and transverse flow velocities in colloidal suspensions using optical coherence tomography," Phys. Rev. E **88**(4), 042312 (2013).
9. J. Lee, W. Wu, J. Y. Jiang, *et al.*, "Dynamic light scattering optical coherence tomography," Opt. Express **20**(20), 22262–22277 (2012).
10. K. Cheishvili and J. Kalkman, "Scanning dynamic light scattering optical coherence tomography for measurement of high omnidirectional flow velocities," Opt. Express **30**(13), 23382–23397 (2022).
11. P. N. Segrè and P. N. Pusey, "Dynamics and scaling in hard-sphere colloidal suspensions," Phys. A **235**(1-2), 9–18 (1997).
12. C. W. J. Beenakker and P. Mazur, "Self-diffusion of spheres in a concentrated suspension," Phys. A **120**(3), 388–410 (1983).
13. C. W. J. Beenakker and P. Mazur, "Diffusion of spheres in a concentrated suspension ii," Phys. A **126**(3), 349–370 (1984).
14. P. N. Segrè and P. N. Pusey, "Scaling of the dynamic scattering function of concentrated colloidal suspensions," Phys. Rev. Lett. **77**(1), 1 (1996).
15. B. Cichocki and B. U. Felderhof, "Time-dependent self-diffusion coefficient of interacting brownian particles," Phys. Rev. A **44**(10), 6551–6558 (1991).
16. A. van Blaaderen, J. Peetermans, G. Maret, *et al.*, "Long-time self-diffusion of spherical colloidal particles measured with flourescence recovery after photobleaching," J. Chem. Phys. **96**(6), 4591–4603 (1992).
17. M. M. Kops-Werkhoven and H. M. Fijnaut, "Dynamic behavior of silica dispersions studied near the optical matching point," J. Chem. Phys. **77**(5), 2242–2253 (1982).
18. M. M. Kops-Werkhoven, C. Pathmamanoharan, and A. Vrij, "Concentration dependence of the self-diffusion coefficient of hard, spherical particles measured with photon correlation spectroscopy," J. Chem. Phys. **77**(12), 5913–5922 (1982).
19. F. Westermeier, B. Fischer, W. Roseker, *et al.*, "Structure and short-time dynamics in concentrated suspensions of charged colloids," J. Chem. Phys. **137**(11), 114504 (2012).
20. J. K. G. Dhont, *An Introduction to Dynamics of Colloids* (Elsevier Science B.V., 1996).
21. A. J. Banchio and G. Nägele, "Short-time transport properties in dense suspensions: From neutral to charge stabilized colloidal spheres," J. Chem. Phys. **128**(10), 104903 (2008).
22. A. J. Banchio, G. Nägele, and J. Bergenholtz, "Collective diffusion, self-diffusion and freezing criteria of colloidal suspensions," J. Chem. Phys. **113**(8), 3381–3396 (2000).
23. P. Baur, G. Nägele, and R. Klein, "Nonexponential relaxation of density fluctuations in charge-stabilized colloids," Phys. Rev. E **53**(6), 6224–6237 (1996).
24. P. N. Segré, O. P. Behrend, and P. N. Pusey, "Short-time brownian motion in colloidal suspensions: Experiment and simulation," Phys. Rev. E **52**(5), 5070 (1995).
25. W. van Megen, R. H. Ottewill, S. M. Owens, *et al.*, "Measurement of the wave-vector dependent diffusion coefficient in concentrated particle dispersions," J. Chem. Phys. **82**(1), 508–515 (1985).

26. B. Cichocki and K. Hinsen, "Dynamic computer simulation of concentrated hard sphere suspensions," Phys. A **187**(1-2), 133–144 (1992).

27. B. Cichocki and K. Hinsen, "Dynamic computer simulation of concentrated hard sphere suspensions," Phys. A **166**(3), 473–491 (1990).

28. U. Genz and R. Klein, "Collective diffusion of charger spheres in the presence of hydrodynamic interaction," Phys. A **171**(1), 26–42 (1991).

29. J. Brady, "The long-time self-diffusivity in concentrated colloidal dispersions," J. Fluid Mech. **272**, 109–134 (1994).

30. P. N. Segré, S. P. Meeker, P. N. Pusey, *et al.*, "Viscosity and structural relaxation in suspensions of hard-sphere colloids," Phys. Rev. Lett. **75**(5), 958 (1995).

31. A. Imhof, A. van Blaaderen, G. Maret, *et al.*, "A comparison between the long-time self-diffusion and low shear viscosity of concentrated dispersions of charged colloidal silica spheres," J. Chem. Phys. **100**(3), 2170–2181 (1994).

32. A. J. Banchio, J. Bergenholtz, and G. Nägele, "Rheology and dynamics of colloidal suspensions," Phys. Rev. Lett. **82**(8), 1792–1795 (1999).

33. *Scattering Methods for Condensed Matter Research: Towards Novel Applications at Future Sources*, vol. 33 of *Lecture Notes of the 43rd IFF Spring School 2012* (Forschungszentrum Jülich GmbH, 2012).

34. A. J. C. Ladd, H. Gang, Z. X. Zhu, *et al.*, "Time-dependent collective diffusion of colloidal particles," Phys. Rev. Lett. **74**(2), 318–321 (1995).

35. A. J. Banchio, M. Heinen, P. Holmqvist, *et al.*, "Short- and long-time diffusion, and dynamic scaling in suspensions of charged colloidal particles," J. Chem. Phys. **148**(13), 134902 (2018).

36. M. S. Wertheim, "Exact solution of the Percus-Yevick integral equation for hard spheres," Phys. Rev. Lett. **10**(8), 321–323 (1963).

37. E. Leutheusser, "Exact solution of the percus-yevick equation for a hard-core fluid in odd dimensions," Phys. A **127**(3), 667–676 (1984).

38. D. J. Kinning and E. L. Thomas, "Hard-sphere interactions between spherical domains in diblock copolymers," Macromolecules **17**(9), 1712–1718 (1984).

39. K. Cheishvili and J. Kalkman, "Sub-diffusion flow velocimetry with number fluctuation optical coherence tomography," Opt. Express **31**(3), 3755–3773 (2023).

40. A. G. Mailer, P. S. Clegg, and P. N. Pusey, "Particle sizing by dynamic light scattering: Non-linear cumulant analysis," J. Phys.: Condens. Matter **27**(14), 145102 (2015).

41. K. N. Clayton, J. W. Salameh, and S. T. Wereley, "Physical characterization of nanoparticle size and surface modification using particle scattering diffusometry," Biomicrofluidics **10**(5), 054107 (2016).

42. R. B. Miles, W. R. Lempert, and J. N. Forkey, "Laser rayleigh scattering," Meas. Sci. Technol. **12**(5), R33–R51 (2001).

43. P. N. Pusey and W. van Megen, "Detection of small polydispersities by photon correlation spectroscopy," J. Chem. Phys. **80**(8), 3513–3520 (1984).

44. G. Nägele and P. Baur, "Long-time dynamics of charged colloidal suspensions: hydrodynamic interaction effects," Phys. A **245**(3-4), 297–336 (1997).

45. W. van Megen and S. M. Underwood, "Tracer diffusion in concentrated colloidal dispersions. iii. mean squared displacements and self-diffusion coefficients," J. Chem. Phys. **91**(1), 552–559 (1989).

46. P. N. Pusey, "Intensity fluctuation spectroscopy of charged brownian particles: the coherent scattering function," J. Phys. A: Math. Gen. **11**(1), 119–135 (1978).

47. J. Buitenhuis, J. K. G. Dhont, and H. N. W. Lekkerkerker, "Static and dynamic light scattering by concentrated colloidal suspensions of polydisperse sterically stabilized boehmite rods," Macromolecules **27**(25), 7267–7277 (1994).

48. P. N. Pusey, H. M. Fijnaut, and A. Vrij, "Mode amplitudes in dynamic light scattering by concentrated liquid suspensions of polydisperse hard spheres," J. Chem. Phys. **77**(9), 4270–4281 (1982).

49. A. van Veluwen, H. N. W. Lekkerkerker, C. G. de Kruif, *et al.*, "Influence of polydispersity on dynamic light scattering measurements on concentrated suspensions," J. Chem. Phys. **89**(5), 2810–2815 (1988).

50. M. Jensen, I. B. Gonzalo, R. D. Engelsholm, *et al.*, "Noise of supercontinuum sources in spectral domain optical coherence tomography," J. Opt. Soc. Am. B **36**(2), A154 (2019).

51. A. Barron and W. Algozeeb, *Physical Methods in Chemistry and Nano Science* (MiDAS Green Innovations, 2020).

52. K. Kolmana, O. Nechyporchuka, M. Perssona, *et al.*, "Preparation of silica/polyelectrolyte complexes for textile strengthening applied to painting canvas restoration," Colloids Surf., A **532**, 420–427 (2017).

53. J. Gapinski, A. Patkowski, A. J. Banchio, *et al.*, "Collective diffusion in charge-stabilized suspensions: Concentration and salt effects," J. Chem. Phys. **126**(10), 104905 (2007).

54. W. C. K. Poon, E. R. Weeks, and C. P. Royall, "On measuring colloidal volume fractions," Soft Matter **8**(1), 21–30 (2012).

55. M. Godin, A. K. Bryan, T. P. Burg, *et al.*, "Measuring the mass, density, and size of particles and cells using a suspended microchannel resonator," Appl. Phys. Lett. **91**(12), 123121 (2007).

56. W. Heller, "Remarks on refractive index of mixture rules," J. Phys. Chem. **69**(4), 1123–1129 (1965).

57. P. Speets and J. Kalkman, "Measuring optical properties of clear and turbid media with broadband spectral interferometry," Appl. Opt. **62**(16), 4349–4358 (2023).

58. *Water refractive index in dependence on temperature and wavelength: A simple approximation*, vol. 5068.

59. I. H. Malitson, "Interspecimen comparison of the refractive index of fused silica," J. Opt. Soc. Am. **55**(10), 1205 (1965).
60. N. Cheng, "Formula for the viscosity of a glycerol−water mixture," Ind. Eng. Chem. Res. **47**(9), 3285–3288 (2008).
61. N. Uribe-Patarroyo, A. L. Post, S. Ruiz-Lopera, *et al.*, "Noise and bias in optical coherence tomography intensity signal decorrelation," OSA Continuum **3**(4), 709–741 (2020).
62. K. Cheishvili, B. Rieger, and J. Kalkman, "Precision and bias in dynamic light scattering optical coherence tomography measurements of diffusion and flow," Biomed. Opt. Express **15**(2), 1288–1310 (2024).
63. J. Kalkman, "Fourier-domain optical coherence tomography signal analysis and numerical modeling," Int. J. Opt. **2017**, 1–16 (2017).
64. W. Schaertl and H. Sillescu, "Brownian dynamics simulations of colloidal hard spheres. effects of sample dimensionality on self-diffusion," J. Stat. Phys. **74**(3-4), 687–703 (1994).
65. J. Kovár and I. Fortelný, "Effect of polydispersity on the viscosity of a suspension of hard spheres," Rheol. Acta **23**(4), 454–456 (1984).
66. R. Besseling, M. Damen, J. Wijgergans, *et al.*, "New unique PAT method and instrument for real-time inline size characterization of concentrated, flowing nanosuspensions," Eur. J. Pharm. Sci. **133**, 205–213 (2019).
67. K. Cheishvili, "Wavenumber-dependent DLS-OCT data and analysis routines," Zenodo 2024 https://doi.org/10.5281/zenodo.8425185.